

02,12

Superconductivity and Phase Diagram in the Nanostructured Eutectic Ga–Ag Alloy

© D.V. Smetanin¹, M.V. Likholetova¹, E.V. Charnaya¹, M.K. Lee^{2,3}, L.J. Chang³, E.V. Shevchenko¹, Yu.A. Kumzerov⁴, A.V. Fokin⁴

¹ Physics Department, St. Petersburg State University, St. Petersburg, Russia

² MOST Instrument Center at NCKU, Tainan, Taiwan

³ Department of Physics, National Cheng Kung University, Tainan, Taiwan

⁴ Ioffe Institute, St. Petersburg, Russia
E-mail: e.charnaya@spbu.ru

Received: April 22, 2022

Revised: April 22, 2022

Accepted: April 25, 2022

Here, we present a study of superconductivity in the Ga–Ag alloy embedded into porous template with pore diameter of 10 nm. The composition was close to the eutectic point in the gallium-rich range. We measured DC and AC magnetizations for temperatures from 1.8 to 10 K and magnetic fields up to 6 T. Three superconducting transitions were found at temperatures 7.05, 6.08, and 2.65 K in contrast to the bulk counterpart. Upper critical field lines were obtained. Activation barriers were evaluated from the AC data. The temperatures of the superconducting transitions were ascribed to emergence of β - and ι -Ga and of an intermetallic different from bulk Ag_3Ga_2 .

Keywords: nanostructured Ga–Ag eutectic alloy, superconducting transitions, segregated phases, DC and AC susceptibility.

DOI: 10.21883/PSS.2022.08.54608.360

1. Introduction

When the dimensions of eutectic alloys are reduced down to the nanometer scale, the concerns arise in the validity of phase diagrams found for their bulk counterparts. Such crucial features as the solubility limits defining the composition ranges of solid solution formation, the solidus temperature, the eutectic point where the liquidus and solidus lines touch with each other, and the symmetry of the precipitated crystalline phases can be generally affected by nanostructuring. Alterations in the phase diagrams influence specific properties of low-dimensional eutectic alloys. These problems attracted great interest long ago; however, they take on a special significance at present when thin wires, films, and small particles of eutectic alloys are considered as promising materials for various applications. The nanostructured metallic eutectic alloys are of particular importance [1–5]. Nevertheless, size effects on the phase diagrams of eutectic alloys are poorly understood. Changes of the eutectic temperatures were studied best of all. Reduction of the solidus temperature was experimentally found in the Ag–Pb, In–Sn, Bi–Sn, and some others binary eutectic alloy nanoparticles, as well as for Ga–In alloy embedded into nanoporous matrices [6–14]. Additionally, remarkable extension of terminal solubility was observed for the Bi–Sn nanoparticles by TEM [15]. Reduction of the melting temperature and

formation of multiphase nanoparticles were seen in the Al–Mg eutectic alloy nanoparticles [16]. Theoretical and experimental studies showed that upon decreasing the size of the Ag–Sn nanoparticles, the eutectic temperature decreased and the eutectic composition moved to the Sn-rich corner [17]. The liquidus line was also shown to deform along with decreasing the melting temperature for the Au–Si nanoscale alloy [18]. Phase and symmetry changes were observed in the Ge–Sn and Ga–In confined nanoparticles [19,20].

Nanostructured eutectic metallic alloys may be used, for instance, in soft robotics, wearable electronics, bio-devices, and self-healing superconductors. Because of their stable electrical properties and non-toxicity, gallium-based alloys were suggested as the most suitable nanomaterials for developing multifunctional devices and elements including nano-superconducting coils, flexible superconducting electronic components, microscale low-temperature nmR, and others. Two gallium nanoalloys, the binary Ga–In and ternary Ga–In–Sn alloys, have great potential. However, even for these nanoalloys, the relation of their superconducting properties and phase diagrams, in particular, symmetries of segregated phases, was not studied. Note that superconductivity of Ga–In–Sn droplets with a mean diameter of 110 nm was observed in [21]. The impact of size reduction on superconductivity in other gallium alloys is almost unknown.

Here, we study superconductivity in the Ga–Ag alloy of eutectic composition embedded into a porous silica glass with an average pore size of 10 nm. The interconnection between the remarkable distinctions of its superconducting properties from those of the bulk alloy and alloy under another nano-confinement, and changes of the phase diagrams is discussed.

2. Samples and experiment

The binary gallium–silver alloy used in the present study consisted of 97 at.% Ga and 3 at.% Ag. This composition is close to the eutectic point at the gallium-rich corner [22]. We used a silica porous glass as a template. The average pore diameter of 10 nm was found by nitrogen porosimetry. The melted alloy was introduced into pores under pressure to achieve the pore filling of $\sim 85\%$. A slab was cut from the filled glass ingot. The sample mass was 38.71 mg.

We measured the DC and AC magnetization of the glass/alloy slab within a temperature range from 1.8 to 10 K using Quantum Design MPMS 3 and PPMS-9, respectively. The DC data were obtained at warming after the sample was cooled down to 1.8 K in zero field (zero field cooled — ZFC protocol) and at successive cooling and warming in field (field cooling cooling — FCC, and field cooling warming — FCW protocols). The AC magnetization measurements were carried out at cooling in different bias fields.

3. Results

3.1. DC magnetization

The dependences of the ZFC susceptibility χ on temperature at several different magnetic fields are shown in Fig. 1. The insets in Fig. 1 show the scaled ZFC and FCC susceptibilities at 10 and 50 Oe to make clear weak changes. The ZFC curve at 10 Oe in Fig. 1 does not reach a plateau while temperature decreases down to the minimal value, however the magnetic screening is near complete at about 1.8 K. The upper inset in Fig. 1 demonstrates three superconducting transitions with critical temperatures $T_{c1} = 7.05$ K, $T_{c2} = 6.08$ K, and $T_{c3} = 2.65$ K. This differs drastically from a single critical temperature of 7.03 K observed for the same Ga–Ag eutectic alloy, embedded into a porous glass with pores of 7 nm [23]. The ZFC and FCC curves in the insets diverge immediately below the first and second superconducting transitions, but run very close to each other at lower temperatures evidencing weak pinning. Below the third phase transitions the ZFC and FCC curves at 10 Oe diverge remarkably, the FCC susceptibility magnitude at lowest temperature is smaller than the ZFC one by more than two orders (Fig. 2). This demonstrates strong pinning of the superconducting vortices below the third transition.

The superconducting transitions shift to low temperatures and diffuse with increasing magnetic field (Fig. 3). The

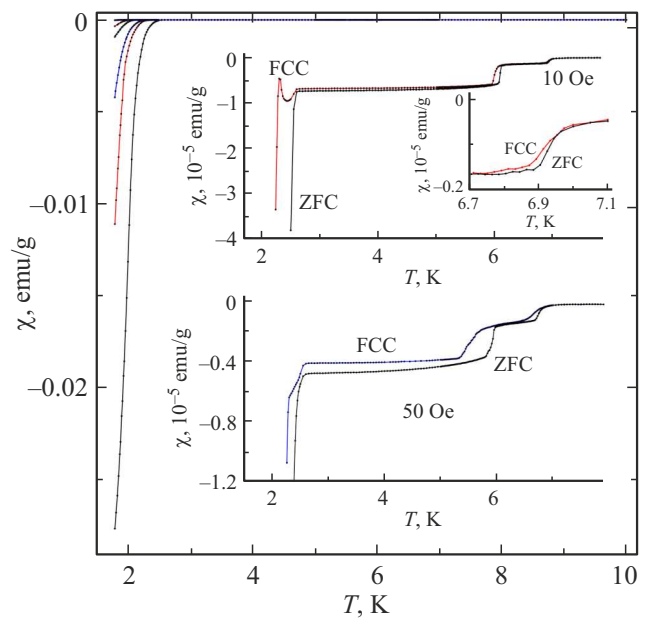


Figure 1. Dependence of DC susceptibility on temperature at applied fields 10, 50, 100, and 500 Oe and 1 and 3 kOe measured under ZFC protocol. The insets show scaled ZFC and FCC susceptibilities at 10 and 50 Oe.

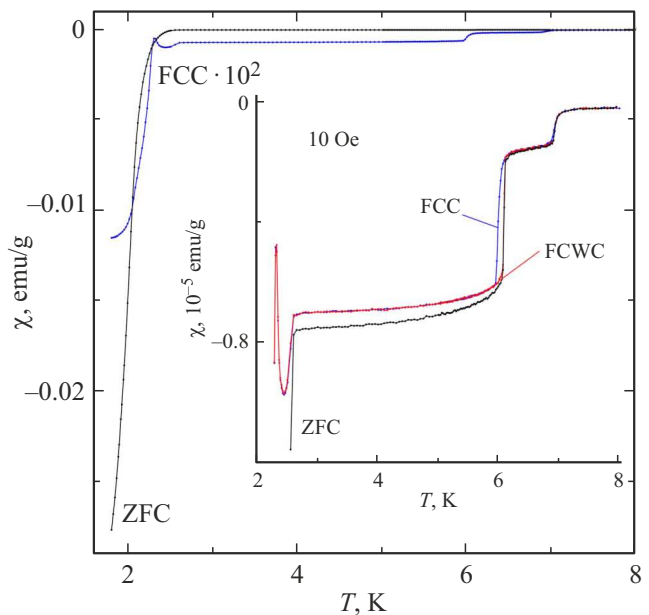


Figure 2. The ZFC and FCC susceptibilities at 10 Oe. The FCC susceptibility is multiplied by 100 for better visibility. The inset shows the scaled ZFC, FCC, and FCW curves obtained at 10 Oe.

temperatures of the first and second transitions decrease faster than in the case of the third transition. As a result, the transitions overlap and gradually merge.

Fig. 3 and the inset at Fig. 2 also show the pronounced hysteresis between the FCC and FCW susceptibilities at magnetic fields up to 100 Oe near the first and second

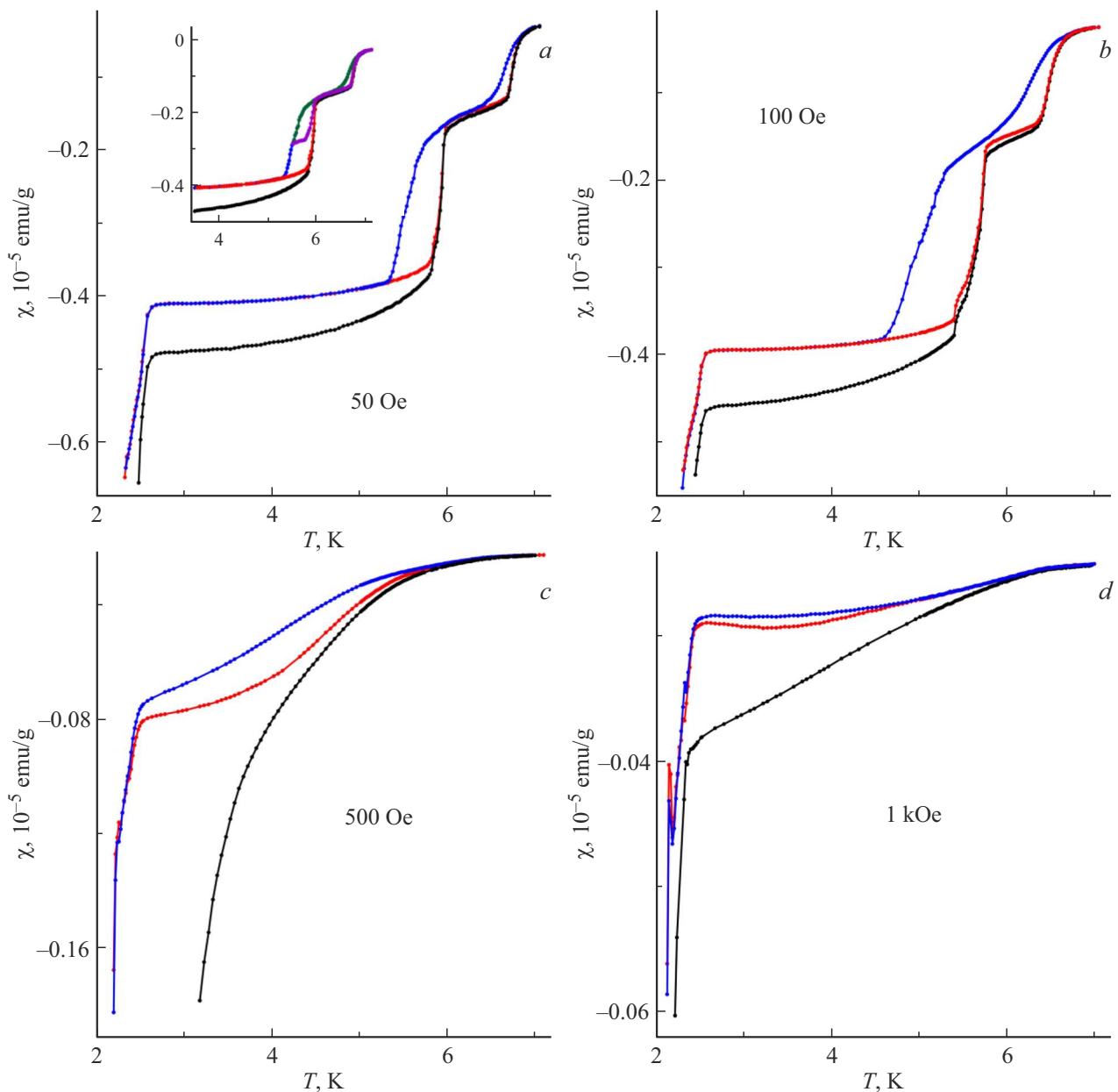


Figure 3. The scaled susceptibilities obtained at a) 50, b) 100, c) 500 Oe, and d) 1 kOe. The black, blue, and red curves are data measured under the ZFC, FCC, and FCW protocols, respectively. The inset in the panel a) shows the results of partial thermal cycles at cooling down to 3.5 and 5.5 K.

transitions. The FCW curves merge with the ZFC ones at temperatures noticeably lower than the FCC and ZFC bifurcation temperatures. This hysteretic behavior is totally reproducible even for partial thermal cycling, as can be seen in the inset to Fig. 3, a. However, the FCC and FCW susceptibilities superimpose at temperatures below the third superconducting transition. For stronger magnetic fields from 500 Oe when the superconducting transitions overlap, the hysteresis between FCC and FCW disappears and the FCC and FCW curves run together apart from the ZFC one.

The dependences of magnetization on magnetic field are presented in Fig. 4 for temperatures below and above

the third transition. The butterfly hysteresis loop at 1.8 K evidences a complex dependence of the critical current on magnetic field and strong pinning. In contrast, the hysteresis loops at 4 and 5 K show partly reversible behavior, which corresponds to weak pinning, in agreement with small differences between the ZFC and FCC magnetizations.

3.2. AC magnetization

Measurements of complex AC magnetization were carried out in different bias magnetic fields at the amplitude of the driving field $H_{AC} = 1$ Oe and several AC frequencies

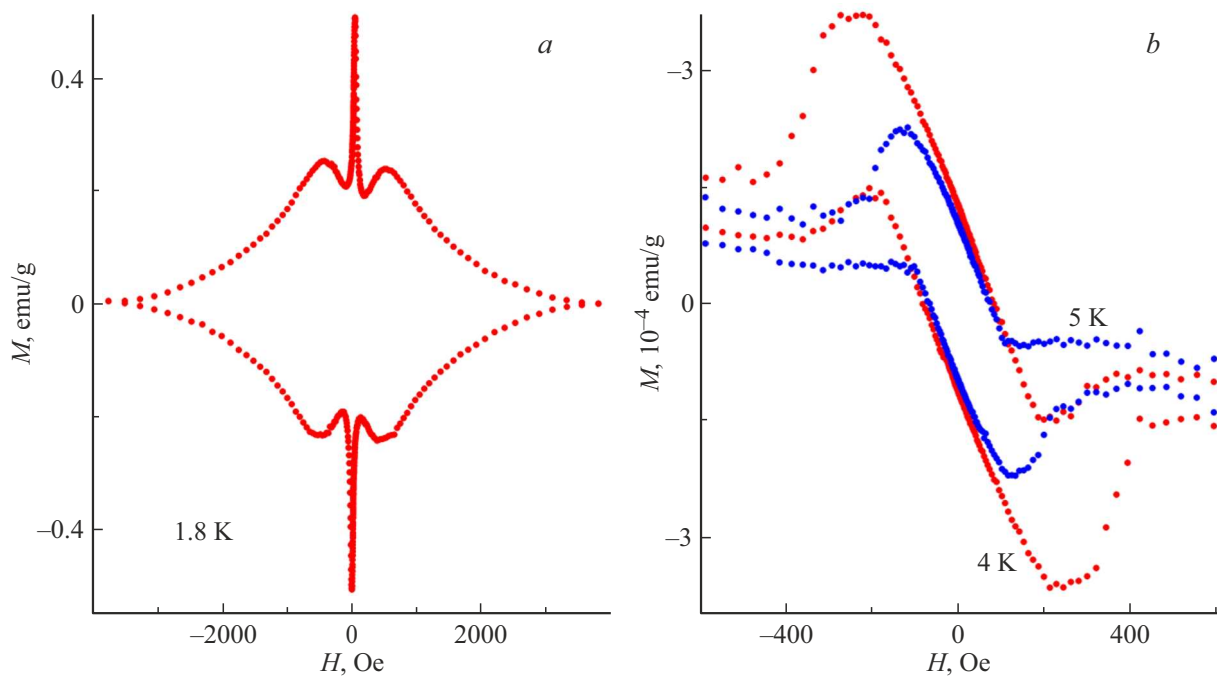


Figure 4. Magnetization isotherms at a) 1.8 K and b) 4 and 5 K.

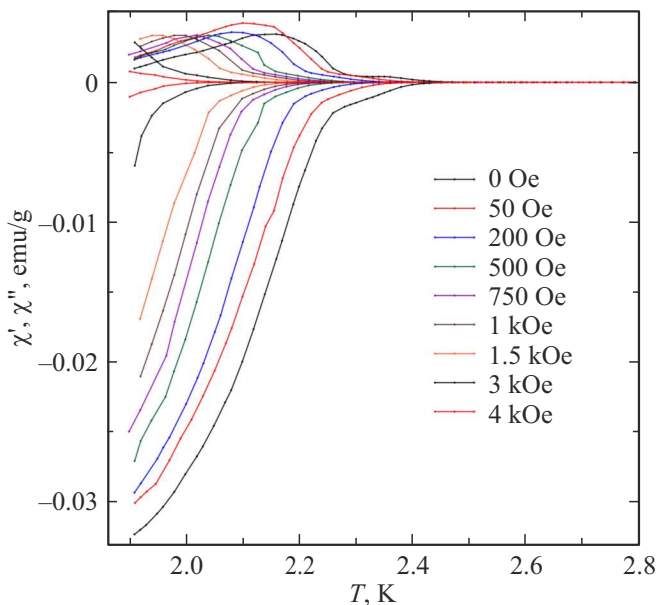


Figure 5. Temperature dependences of the imaginary and real parts of AC susceptibility obtained at frequency 1 kHz and AC amplitude 1 Oe in bias fields indicated in the panel from right to left.

in the range from 90 Hz to 7 kHz. Additional AC data were obtained in zero bias field at a frequency of 1 kHz and various H_{AC} . The temperature dependences of the real χ' and imaginary χ'' parts of susceptibility are shown in Fig. 5. The imaginary parts consist of two humps, a rather weak high temperature hump, and a stronger low-

temperature one. The real parts at low magnetic fields, especially at zero field, confirm the complex AC losses. This suggests that the third superconducting transition has two stages with different critical temperatures. Such a suggestion explains the behavior of ZFC and FCC DC susceptibilities at relatively small fields, which deviate simultaneously from their weak temperature dependences above the transition, but have a pronounced shift at cooling further (see insets in Fig. 1). Note that the critical temperatures found for the third transition from the DC data correspond to the onset of the higher-temperature stage. No reliable peaks of the imaginary parts of AC susceptibility were observed within the temperature ranges of the first and second transitions in agreement with faint DC magnetization changes within the temperature ranges of these transitions.

High sensitivity of AC susceptibility to the value of H_{AC} (Fig. 6) along with weak sensitivity to driving frequency corresponds to the thermally assisted vortex mobility [24,25]. In this case, a particular power dependence is predicted for the AC amplitude as a function of temperature T_p of AC losses peak in granular superconductors [26–28]. The inset in Fig. 6 illustrates such a dependence $H_{AC} \sim (1 - T_p/T'_{c3})^\beta$ with $\beta = 3.6$. Here, T'_{c3} was assumed to coincide with the onset of the second stage of the third superconducting transition and was equal to 2.29 K. The exponent β is higher than was found in [28]; however, it agrees with the results obtained in [23].

The shift of the peak temperature T_p with AC frequency follows the Arrhenius law (not shown) at all bias fields. This allows us to evaluate the vortex activation barriers U_a , which variations with magnetic field are shown in the inset

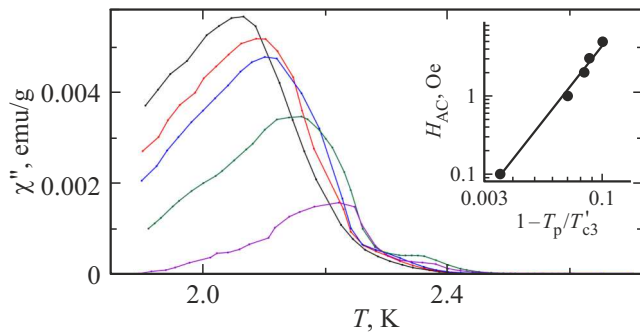


Figure 6. The imaginary part of AC susceptibility measured at the AC amplitude (bottom-up) 0.1, 1, 2, 3, and 5 Oe and frequency 1 kHz. The inset illustrates the shifts of the peak position T_p at different AC amplitudes.

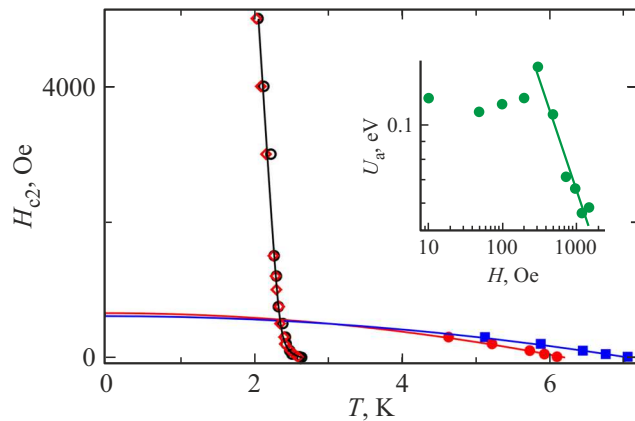


Figure 7. The temperature dependences of the upper critical fields for the first (squares), second (closed circles) and third (open circles and diamonds) superconducting transitions. Open circles and diamonds correspond to AC and DC data, respectively. Solid lines for the first and second transitions are fitting curves for the two-liquid model. Solid line for the third transition represents the proximity effect model [45]. The inset shows the dependence of activation barrier on the bias field.

in Fig. 7. A weak dependence of U_a on field below 300 Oe accelerates at higher field and changes to $U_a \sim H^{-0.62}$. Remarkable drops of activation barriers with increasing field were reported for bulk and nanocomposite superconductors [29–30]. In some nanocomposites, the bend on the $U_a(H)$ dependence correlated with the curvature crossover field on the phase diagram. However, for the nanocomposite under study the crossover field is quite uncertain while it is higher than 300 Oe. We can suggest that the first and second superconducting transitions affect strongly the transformations in the vortex system within the temperature range of the third transition. In addition, the two-steps character of this transition, which yields the double humps on the imaginary parts of AC magnetization, can also influence the vortex system.

The phase diagram in Fig. 7 shows the upper critical field lines found from the DC magnetization measurements

for the first and second superconducting transitions, and from the AC and DC data for the third transition. The AC data correspond to the onset of the first stage. The DC data were obtained from ZFC measurements. The critical lines for the first and second transitions can be extended only up to 300 Oe because of broadening and overlapping the transitions at stronger fields. The curvature of these two lines is weakly negative. The upper critical line for the third transition demonstrates the positive curvature at low magnetic fields and tends to the downturn at increasing field.

4. Discussion

Superconductivity in bulk Ga–Ag alloys was studied in [33,34]. The superconducting transitions within the interval 6.5 to 8 K were observed for alloys with intermediate amount of gallium from 20 up to 70 at.% [33]. The high critical temperatures corresponded to the segregation of gallium–silver intermetallic compounds. No transitions were reported down to 1.6 K for smaller and larger gallium concentrations. The Ga-poor compositions demonstrated superconducting transitions below 120 mK [34]. The recent studies of the phase diagram for bulk Ga–Ag specified that two crystalline phases in the Ga-rich alloys are almost pure gallium with α -Ga structure and Ag_3Ga_2 intermetallic with space symmetry $Pmmm$ [35,36].

Superconductivity in a nanocomposite consisting of a porous glass with pores of 7 nm filled with the Ga–Ag alloy of the composition is close to the eutectic one that was studied in [23]. The only one superconducting transition was observed at 7.03 K. This transition secured the almost complete shielding of the nanocomposite volume at low magnetic fields. The high transition temperature compared to that in α -Ga (1.08 K) was ascribed to the formation of ι -Ga, which occurs under nanoconfinement [37].

Figs. 1 and 4 confirm that the nanocomposite under study belongs to type II superconductors as was observed for other composites based on nanoporous templates [31,32,38]. The Ga–Ag alloy forms within pores a network of nanoparticles with dendritic shape [32]. However, in contrast to [23], the use of the porous glass with 10 nm pores leads to the appearance of three superconducting transitions above 1.8 K. The first transition has a temperature of 7.05 K, which is very close to that observed in [23]. The second transition temperature is a little lower, 6.08 K. It coincides within the experimental accuracy with the superconducting transition of β -Ga [39,40], which is metastable in bulk but stabilizes under nanoconfinement [41]. The fraction of these two phases is very small as the ratio of magnetizations at 3 and 1.8 K is only $\approx 2 \cdot 10^{-4}$. We can suggest that a small amount of non-linked dendritic nanoparticles within pores freezes in ι -Ga and β -Ga. The pinning of superconducting vortices is weak owing to the homogeneous structure of dendritic particles, which correlates with the partly reversible hysteresis loops (Fig. 4). The

superconducting transition at 2.65 K was never observed for bulk or nanostructured gallium [37]. Then we may assume that the major part of the gallium-rich precipitate has the α -Ga structure. The second segregated phase in the bulk gallium-rich Ga–Ag alloy was recently identified as the Ag_3Ga_2 intermetallic compound [35]. However, according to the results obtained in [33], the bulk Ga–Ag alloy did not show superconducting transitions down to 1.6 K for gallium composition larger than 70 at.%. Therefore, the Ag_3Ga_2 compound, which occurs in the solid alloy when gallium composition is higher than 40 at%, cannot respond for superconductivity below 2.65 K in our sample. We can assume that another intermetallic emerges under the particular nanoconfinement in the crystalline Ga–Ag alloy and induces superconductivity with the critical temperature 2.65 K.

The hysteresis between the FCC and FCW curves was observed only near the first and second superconducting transitions. It was very reproducible as can be seen from the example shown in the inset to Fig. 3, *a*. Its specific feature is the approach of the FCW susceptibility to the ZFC curve in such a way that the hysteresis loop is formed by the FCC susceptibility from the low-temperature side and by merged FCW and ZFC curves from the high-temperature side. Such hysteresis loops were predicted in [42] using the critical current concept and were reported occasionally for some type-II superconductors [43]. However, they were not found for superconducting nanocomposites consisted of nanoporous templates loaded with metals or alloys. Note, that another kind of hysteretic behavior between the FCC and FCW magnetizations was demonstrated in [23], the FCC curve running below the FCW one.

The upper critical lines for the first and second transitions on the phase diagram have ordinary negative curvature (Fig. 7). They can be fitted by the two-fluid model, which gives us the values of the upper critical fields at zero temperature $H_{c2}(0)$ equal to ~ 610 and 650 Oe for the first and second transitions, respectively. According to our suggestion, the second transition is due to a small amount of dendritic particles with the β -Ga structure. The upper critical field for β -Ga is ~ 570 Oe [44], which is quite close to our estimate of 650 Oe. The upper critical field for ι -Ga was not reported. Thus, the value 610 Oe is the only estimate for it.

The upper critical line for the onset of the third superconducting transition has a positive curvature [Fig. 7]. The positive curvature weakens at increasing field. The upward critical lines were observed in various bulk type-II superconductors and in some composites with metallic nanoparticles (see [23,31,32] and references therein). It was suggested in [32] that the upturn dependence of the critical field on temperature for such nanocomposites is related to their morphology, which can be modeled as granular superconductors with strong and weak links. The proximity effect was found in [45] to cause the positive curvature of the upper critical line transforming to the negative one with increasing field. Using the relationships obtained

in [45], we fitted the critical line for the third transition as shown in Fig. 7.

Conclusion

Superconductivity in the Ga–Ag alloy of the eutectic composition embedded into porous glass with pores of 10 nm differs drastically from that in the same alloy embedded into porous glass with smaller pore size of 7 nm [23]. While a single superconducting transition at 7.03 K was observed in the nanocomposite based on porous glass with pore size of 7 nm, three superconducting transitions were found in the nanocomposite studied in the present paper at temperatures $T_{c1} = 7.05$ K, $T_{c2} = 6.08$ K, and $T_{c3} = 2.65$ K at 10 Oe. Only small fractions of the nanocomposite were screened from magnetic field as a result of the first and second superconducting transitions. In contrast, the third transition with a critical temperature of 2.65 K leads to almost complete shielding of the nanocomposite volume from magnetic field. The results obtained in the present paper show remarkable changes of the phase diagram for the nanostructured Ga–Ag alloy compared to the bulk counterpart. The found temperatures of the superconducting transitions indicate the formation within pores of small amounts of the gallium rich precipitate with ι -Ga structure, which occurs under nanoconfinement, and with the symmetry of β -Ga. The dominant superconducting properties are due to an intermetallic, which differs from the Ag_3Ga_2 compound segregated in the bulk Ga–Ag alloy.

Funding

The present study was supported by RSF (Russia), grant 21-72-20038. Measurements were carried out using the equipment of the Resource Centre „Centre for Diagnostics of Functional Materials for Medicine, Pharmacology, and Nanoelectronics“, Research Park of St.Petersburg State University.

Conflicts of interests

The authors declare that they have no conflict of interest.

References

- [1] J. Tang, R. Daiyan, M.B. Ghasemian, S.A. Idrus-Saidi, A. Zavabeti, T. Daeneke, J. Yang, P. Koshy, S. Cheong, R.D. Tilley, R.B. Kaner, R. Amal, K. Kalantar-Zadeh. *Nature Commun.* **10**, 1, 4645 (2019).
- [2] Z. Li, Y. Guo, Y. Zong, K. Li, S. Wang, H. Cao, C. Teng. *Nanomater.* **11**, 9, 2246 (2021).
- [3] *Metallic Nanostructures. From Controlled Synthesis to Applications* / Ed. Y. Xiong, X. Lu. Springer International Publishing (2015).
- [4] M. Tavakoli, M.H. Malakooti, H. Paisana, Y. Ohm, D.G. Marques, P.A. Lopes, A.P. Piedade, A.T. de Almeida, C. Majidi. *Adv. Mater.* **30**, 29, 1801852 (2018).

- [5] G. Bo, L. Ren, X. Xu, Y. Du, S. Dou. *Adv. Phys. X* **3**, *1*, 1446359 (2018).
- [6] C.L. Chen, J.-G. Lee, K. Arakawa, H. Mori. *Appl. Phys. Lett.* **98**, *8*, 083108 (2011).
- [7] H. Lu, J. Shuai, X. Meng. *J. Nanosci. Nanotechnol.* **13**, *2*, 1480 (2013).
- [8] J.G. Lee, H. Mori, H. Yasuda. *Phys. Rev. B* **65**, *13*, 132106 (2002).
- [9] H. Adhikari, A.F. Marshall, I.A. Goldthorpe, C.E.D. Chidsey, P.C. McIntyre. *ACS Nano* **1**, *5*, 415 (2007).
- [10] E. Sutter, P. Sutter. *Nano Lett.* **8**, *2*, 411 (2008).
- [11] E.J. Schwalbach, P.W. Voorhees. *Nano Lett.* **8**, *11*, 3739 (2008).
- [12] B.J. Kim, J. Tersoff, C.Y. Wen, M.C. Reuter, E.A. Stach, F.M. Ross. *Phys. Rev. Lett.* **103**, *15*, 155701 (2009).
- [13] W.A. Jesser, R.Z. Shneck, W.W. Gile. *Phys. Rev. B* **69**, *14*, 144121 (2004).
- [14] A.L. Pirozerskii, E.V. Charnaya, M.K. Lee, L.J. Chang, A.I. Nedbai, Y.A. Kumzerov, A.V. Fokin, M.I. Samoilovich, E.L. Lebedeva, A.S. Bugaev. *Acoust. Phys.* **62**, *3*, 306 (2016).
- [15] G.L. Allen, W.A. Jesser. *J. Cryst. Growth* **70**, *1-2*, 546 (1984).
- [16] L.S. Kumar, S.R. Chakravarthy, R. Verma, R. Jayaganthan, R. Sarathi, A. Srinivasan. *J. Alloys Compd.* **838**, *15*, 155630 (2020).
- [17] K. Sim, J. Lee. *J. Alloys Compd.* **590**, 140 (2014).
- [18] B.J. Kim, J. Tersoff, C.-Y. Wen, M.C. Reuter, E.A. Stach, F.M. Ross. *Phys. Rev. Lett.* **103**, *15*, 155701 (2009).
- [19] S.J. Shin, J. Guzman, C.-W. Yuan, C.Y. Liao, C.N. Boswell-Koller, P.R. Stone, O.D. Dubon, A.M. Minor, M. Watanabe, J.W. Beeman, K.M. Yu, J.W. Ager, D.C. Chrzan, E.E. Haller. *Nano Lett.* **10**, *8*, 2794 (2010).
- [20] E.N. Latysheva, A.L. Pirozerskii, E.V. Charnaya, Yu.A. Kumzerov, A.V. Fokin, A.I. Nedbai, A.S. Bugaev. *Phys. Solid State* **57**, *1*, 131 (2015).
- [21] L. Ren, J. Zhuang, G. Casillas, H. Feng, Y. Liu, X. Xu, Y. Liu, J. Chen, Y. Du, L. Jiang, S.X. Dou. *Adv. Func. Mater.* **26**, *44*, 8111 (2016).
- [22] A.E. Gunnaes, O.B. Karlsen, A. Olsen, P.T. Zagierski. *J. Alloys Compd.* **297**, *1-2*, 144 (2000).
- [23] E.V. Shevchenko, E.V. Charnaya, M.K. Lee, L.-J. Chang, M.V. Likholetova, I.E. Lezova, Y.A. Kumzerov, A.V. Fokin. *Physica C* **574**, 1353666 (2020).
- [24] T.T.M. Palstra, B. Batlogg, R.B. van Dover, L.F. Schneemeyer, J.V. Waszczak. *Phys. Rev. B* **41**, *10*, 6621 (1990).
- [25] G. Prando, P. Carretta, R. De Renzi, S. Sanna, A. Palenzona, M. Putti, M. Tropeano. *Phys. Rev. B* **83**, *17*, 174514 (2011).
- [26] E.H. Brandt. *Phys. Rev. B* **55**, *21*, 14513 (1997).
- [27] F. Gömöry. *Supercond. Sci. Technol.* **10**, *8*, 523 (1997).
- [28] J.R. Clem, B. Bumble, S.I. Raider, W.J. Gallagher, Y.C. Shih. *Phys. Rev. B* **35**, *13*, 6637 (1987).
- [29] G. Prando, P. Carretta, R. De Renzi, S. Sanna, H.-J. Grafe, S. Wurmehl, B. Büchner. *Phys. Rev. B* **85**, *14*, 144522 (2012).
- [30] S.R. Ghorbani, X.L. Wang, M. Shabazi, S.X. Dou, K.Y. Choi, C.T. Lin. *Appl. Phys. Lett.* **100**, *7*, 072603 (2012).
- [31] M.K. Lee, E.V. Charnaya, C. Tien, L.J. Chang, Y.A. Kumzerov. *J. Appl. Phys.* **113**, *11*, 113903 (2013).
- [32] M.K. Lee, E.V. Charnaya, S. Mühlbauer, U. Jeng, L.J. Chang, Y.A. Kumzerov. *Sci. Rep.* **11**, *1*, 4807 (2021).
- [33] N.E. Alekseevskii. *Sov. Phys. JETP* **22**, *1*, 114 (1966).
- [34] R.F. Hoyt, A.C. Mota, C.A. Luengo. *Phys. Rev. B* **14**, *2*, 441 (1976).
- [35] Y. Zhang, J.B. Li, J.K. Kiang, Q.L. Liu, Y.G. Xiao, Q. Zhang, G.H. Rao, C.R. Li. *Calphad* **30**, *3*, 316 (2006).
- [36] D. Jendrzejczyk-Handzlik, P. Handzlik, K. Fitzner. *J. Phase Equilib. Diffus.* **40**, *64* (2019).
- [37] E.V. Charnaya, C. Tien, M.K. Lee, Y.A. Kumzerov. *J. Phys.: Condes. Matter* **21**, *45*, 455304 (2009).
- [38] C. Tien, E.V. Charnaya, D.Y. Xing, A.L. Pirozerskii, Yu.A. Kumzerov, Y.S. Ciou, M.K. Lee. *Phys. Rev. B* **83**, *1*, 014502 (2011).
- [39] D. Teske, J.E. Drumheller. *J. Phys.: Condes. Matter* **11**, *25*, 4935 (1999).
- [40] H. Parr. *Phys. Rev. B* **10**, *11*, 4572 (1974).
- [41] D.Y. Nefedov, E.V. Charnaya, A.V. Uskov, A.O. Antonenko, D.Yu. Podorozhkin, J. Haase, Yu.A. Kumzerov, A.V. Fokin. *Appl. Magn. Res.* **52**, *12*, 1721 (2021).
- [42] J.R. Clem, Z. Hao. *Phys. Rev. B* **48**, *18*, 13774 (1993).
- [43] S. Sundar, M.K. Chattopadhyay, L.S.S. Chandra, S.B. Roy. *Supercond. Sci. Technol.* **28**, *7*, 075011 (2015).
- [44] D. Campanini, Z. Diao, A. Rydh. *Phys. Rev. B* **97**, *18*, 184517 (2018).
- [45] S. Theodorakis, Z. Teanovic. *Phys. Rev. B* **40**, *10*, 6659 (1989).